Supporting Information for "Electron-phonon coupling in a magic-angle twisted-bilayer graphene device from gate-dependent Raman Spectroscopy and atomistic modeling"

Andreij C. Gadelha[1,2,††], Viet-Hung Nguyen[3,††], Eliel G. S. Neto[4],

Fabiano Santana[1], Markus B. Raschke[2], Michael Lamparski[5],

Vincent Meunier[5], Jean-Christophe Charlier[3,*] and Ado Jorio[1†]

[1]*Physics Department, Universidade Federal de Minas Gerais,*

Belo Horizonte, MG, 31270-901, Brazil.

[2]*Department of Physics, and JILA,*

University of Colorado at Boulder, Boulder, Colorado 80309, USA.

[3]*Institute of Condensed Matter and Nanosciences,*

Université catholique de Louvain (UCLouvain), Louvain-la-Neuve, Belgium.

[4]*Physics Institute, Universidade Federal da Bahia, Salvador - BA, 40170-115 Brazil.*

[5]*Department of Physics, Applied Physics, and Astronomy,*

Jonsson Rowland Science Center, Troy, NY, USA. and

[††] *These two authors contributed equally to this work.*

(Dated: July 19, 2022)

Abstract

This supplementary material to the work entitled "Electron-phonon coupling in a magic-angle twisted-bilayer graphene device from gate-dependent Raman Spectroscopy and atomistic modeling" brings more details about the theory, including structural relaxation and phonon calculations, the electronic models, the modeling of Phonon Kohn anomalies and comment about the limited doping range calculations for magic-angle twisted-bilayer graphene. It also brings further experimental information, including details about the D, G and 2D (or G′) band spectra and spectral fitting, device structure and characterization.

1

1. Theoretical Supporting Information

1.1. Structural relaxation and phonon calculations

We use classical force-fields for structural relaxation and to compute the corresponding phonons in the harmonic approximation [1]. Intralayer forces are computed using the second-generation REBO potential, while interlayer forces are modeled using the registry-dependent Kolmogorov-Crespi potential, in its local normal formulation. All atomic positions and lattice parameters of the superlattice are optimized with a conjugate gradient algorithm. The latter are found to vary in a negligible manner compared to the rigidly stacked case. After all atomic positions and superlattice parameters were optimized until all force components are less than 1 meV/atom, the phonon and electronic structures are computed.

1.2. Electronic models

Similar to those performed in [2, 3], the electronic structure of the considered graphene bilayer systems was computed using the p_z tight-binding (TB) Hamiltonians and the lattice relaxation is fully taken into account. Hopping energies t_{nm} between carbon sites are determined by the standard Slater-Koster formula

$$t_{nm} = \cos^2 \phi_{nm} V_{pp\sigma}(r_{nm}) + \sin^2 \phi_{nm} V_{pp\pi}(r_{nm}) \tag{S1}$$

where the direction cosine of $\vec{r}_{nm} = \vec{r}_m - \vec{r}_n$ along Oz axis is $\cos \phi_{nm} = z_{nm}/r_{nm}$. The distance-dependent Slater-Koster parameters are determined as [6]

$$V_{pp\pi}(r_{nm}) = V_{pp\pi}^0 \exp\left[q_\pi \left(1 - \frac{r_{nm}}{a_0} \right) \right] F_c(r_{nm})$$

$$V_{pp\sigma}(r_{nm}) = V_{pp\sigma}^0 \exp\left[q_\sigma \left(1 - \frac{r_{nm}}{d_0} \right) \right] F_c(r_{nm})$$

with a smooth cutoff function $F_c(r_{nm}) = \left[1 + \exp\left(\frac{r_{nm}-r_c}{\lambda_c} \right) \right]^{-1}$. In this work, we particularly used

$$V_{pp\pi}^0 = -2.7\,eV, \ \ V_{pp\sigma}^0 = 367.5\,meV,$$

$$\frac{q_\pi}{a_0} = \frac{q_\sigma}{d_0} = 22.18\,nm^{-1},$$

$$a_0 = 0.142\,nm, \ \ d_0 = 0.343\,nm, \ \ r_c = 0.614\,nm, \ \ \lambda_c = 0.0265\,nm$$

In addition, in order to accurately model the features related the electron-hole asymmetry in graphene systems, the present tight-binding Hamiltonian considers the 1st and 2nd neighbors hopping integrals with opposite signs [4, 5]. Indeed, similarly as computed in [2, 3] with the structure relaxation taken into account, this tight-binging Hamiltonian accurately models the almost flat bands of twisted bilayer graphene at the magic angle as experimentally observed in Refs. [2, 7].

At low angles (i.e., around and below 1.1°), twisted bilayer graphene systems present large spatial variation and strong electron localization in AA stacking regions at low energies [3], leading to strong charge inhomogeneities within the moiré unit cell. As a consequence, strong Coulomb interactions appear in these cases and have been demonstrated to smoothen and therefore diminish the mentioned charge inhomogeneities, especially, when the system is
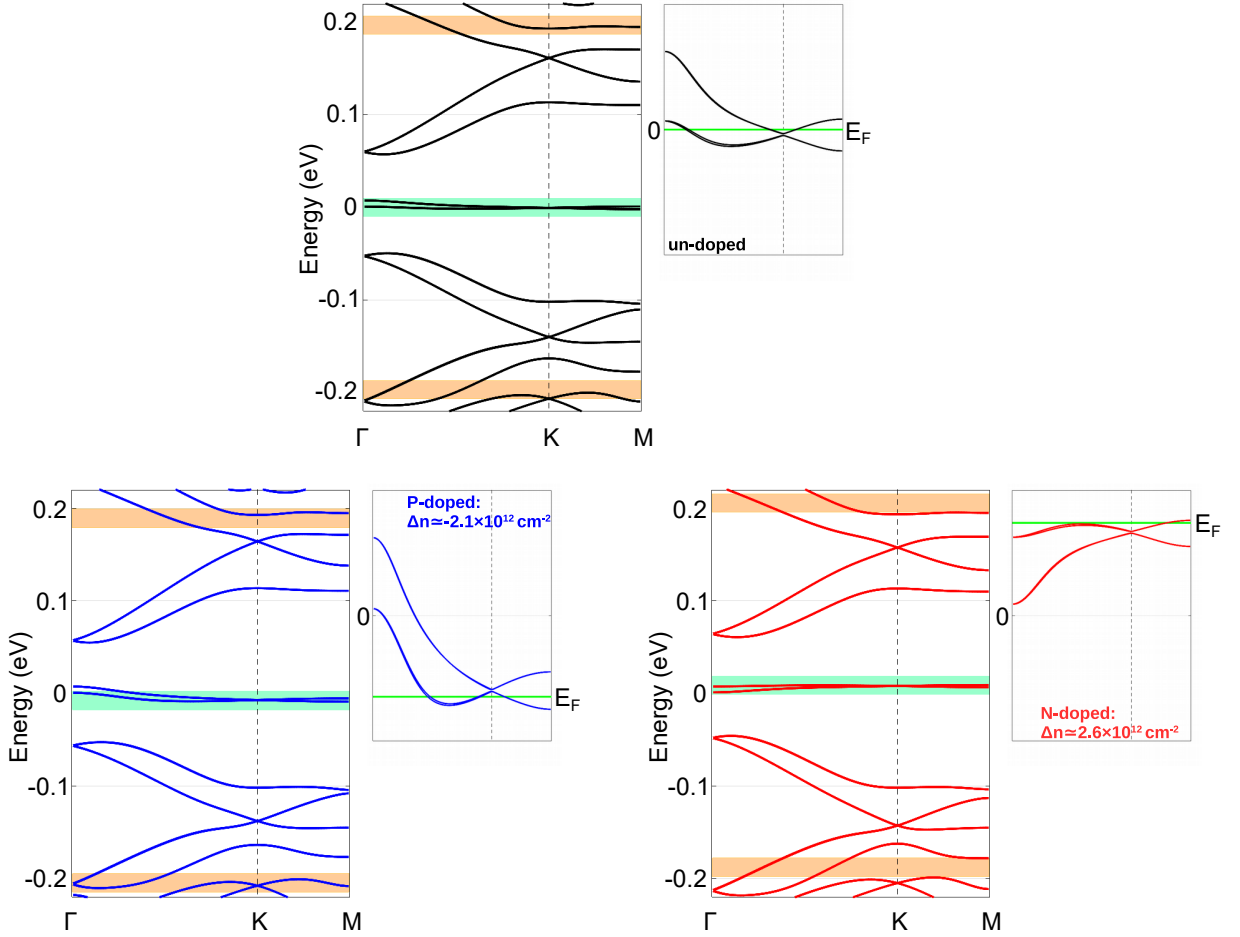
FIG. S1: **Doping effects on the electronic structure of magic-angle twisted bilayer graphene.**

doped [8–13]. To effectively compute these effects at the magic-angle, the single particle TB Hamiltonian described above is adjusted by adding onsite energies, which is determined by the Hartree potential energy $V_H(\vec{r})$ [10, 11]. This Hartree potential function has actually been shown to be dependent of twist angle and doping as well as the environmental screening effects [11]. As a simple approximation, $V_H(\vec{r})$ has the following form [8, 11]

$$V_H(\vec{r}) \simeq V_{MA}(\Delta n_e) \sum_{j=1,2,3} \cos(\vec{G}_j \vec{r}) \tag{S2}$$

where $\vec{G}_j$ denote three reciprocal vectors and V_{MA} is a almost linear function of doping concentration Δn_e. The presence of this Hartree potential can be modeled by estimating its difference ΔV_H in the center of the AA and AB stacking regions. In particular, we used V_{MA} = $\beta \Delta n_e$ with $\beta \simeq -2.86 \times 10^{-12}$ meV cm^2, i.e., yielding $\Delta V_H \simeq 41$ meV for $\Delta n_e = 3 \times 10^{12}$ cm^{-2}, that is close to the value estimated in [11] for magic-angle twisted system.

Thus, while it is neglected in the large-angle twisted and Bernal stacking bilayer graphene cases, the above Hartree potential energy was added to the TB Hamiltonian to effectively model the electronic properties of doped twisted bilayer graphene at the magic-angle as illustrated in Fig. S1 here and Fig. 3 of the main text. Indeed, this empirical TB Hamiltonian can produce the doping effects on the electronic structure of magic-angle twisted
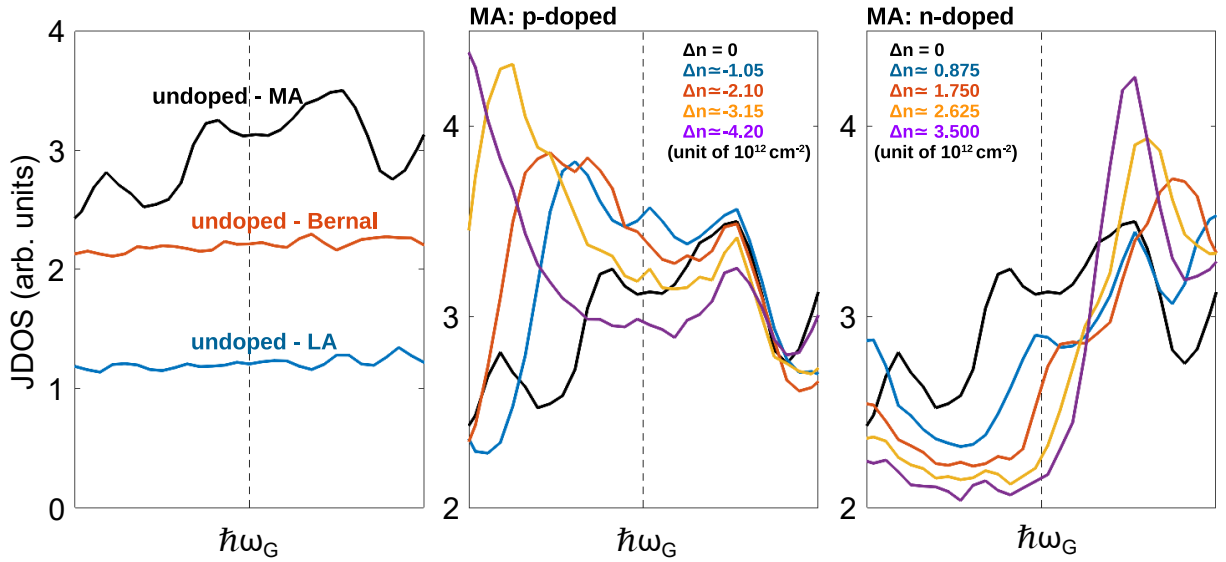
FIG. S2: **JDOS($\hbar\omega_G$) computed at different doping levels:** undoped case for the three bilayer graphene systems (left panel) as in Fig.2, p-doped (central panel) and n-doped (right panel) cases for the magic-angle twisted bilayer system.

system that are in good agreement with those obtained in the published works [8–13] using self-consistent calculations. Indeed, calculations based on this model interpret well the experimental observation of G-band linewidth as presented in our paper.

In Fig. S2, the joint density of states around the energy of G-phonon bands ($\hbar\omega_G$) is computed and presented for bilayer graphene systems investigated in this work. The presented results clearly illustrate the role of different electronic structures in explaining the different behaviors of Γ_G observed in these graphene systems.

1.3. Modeling Phonon Kohn anomalies

In this work, our numerical investigation focuses on the modeling of G-band phonons and therefore was performed for the optical phonon modes. We notice that in twisted bilayer graphene systems, the moiré interlayer potential, on the one hand, presents significant influences on the vibration properties [1, 2] and, on other hand, would cause the phonon band folding [14]. Due to the latter, the number of optical phonon eigenstates in calculations
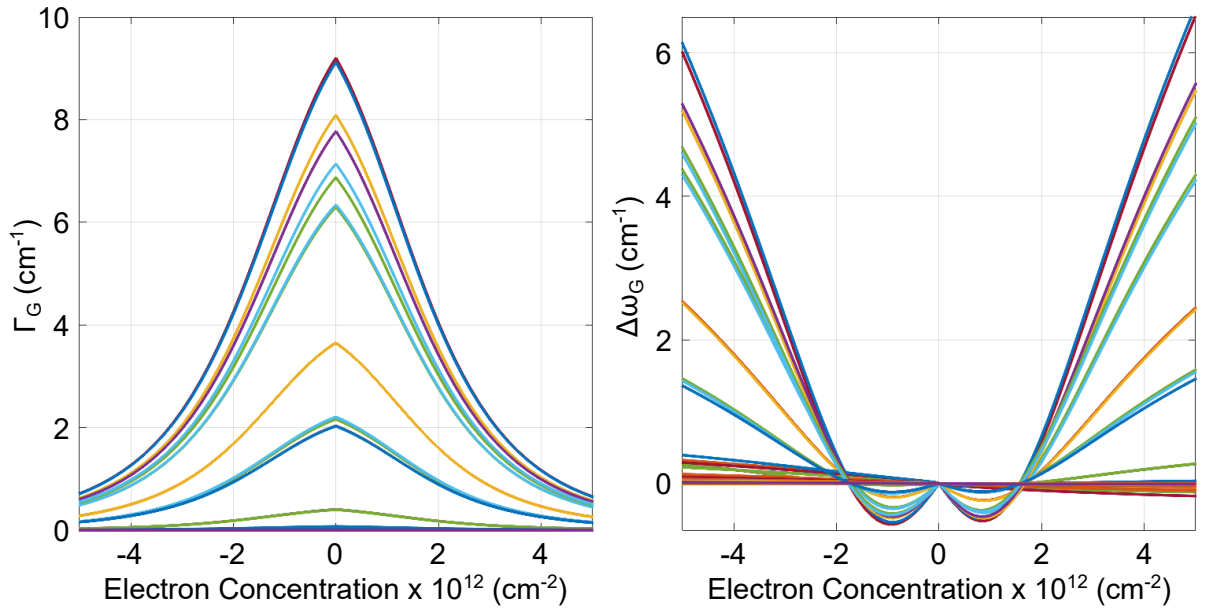
FIG. S3: **Phonon linewidth (left) and frequency shift (right) computed for different optical (G) phonon modes in a large angle ($\sim 7°$) twisted bilayer graphene.** The curves in different colors are obtained for highest energy phonons, i.e., optical G-band phonons, all of them have $\hbar\omega_G \approx 197$ meV.

rapidly increases in twisted systems, especially, is huge at the magic-angle. Because of this issue and to properly model the properties of G-band phonons, we performed our calculations for highest energy optical phonons, particularly, 100 highest energy optical phonon modes are computed for twisted bilayer graphene systems.

In addition, among those computed phonon modes, there are several modes that are Raman-inactive (or weakly active). This is clearly illustrated in Fig. S3 showing our numerical results in the large-angle twisted bilayer system, i.e., inactive models present relatively small value of their linewidth. Note that the phonon linwidth in Fig. S3 is plotted without adding the intrinsic width Δ as done for Fig. 2. Therefore, in order to interpret the experimental data, the numerical results in Fig. 2 are obtained weighted by factors that filter out these Raman-inactive modes.

1.4. Limited Doping Range Calculations for Magic-Angle Twisted Bilayer Graphene

In Fig.2(b) of main paper, we do not extend the calculations for higher carrier doping values because the applied theoretical approach is valid only in the regime where the flat bands of magic-angle TBG are being occupied/emptied. In the larger doping regime, when
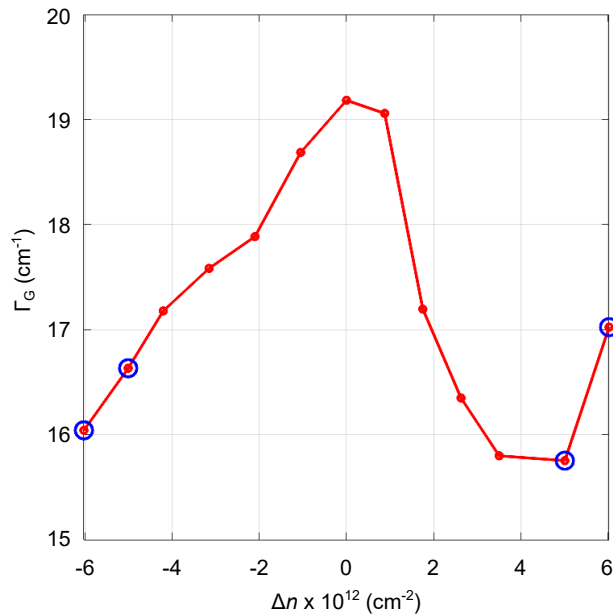
FIG. S4: **Extending the calculations shown in Fig.2(b) of the main paper**. The red bullets are the same data as in Fig.2(b) (red line), while the red bullets circled by blue circles are the extended data, expected to be inadequate due to the failure of the model.

high energy (i.e., dispersive) bands can be largely occupied, more complicated models of Hartree potentials should be considered. However, for completeness, figure S4 includes four more points at higher and lower doping ranges (see circled bullets), but emphasizing that the behavior is expected to be inadequate.

2. Experimental Supporting Information

2.1. Raman spectroscopy data
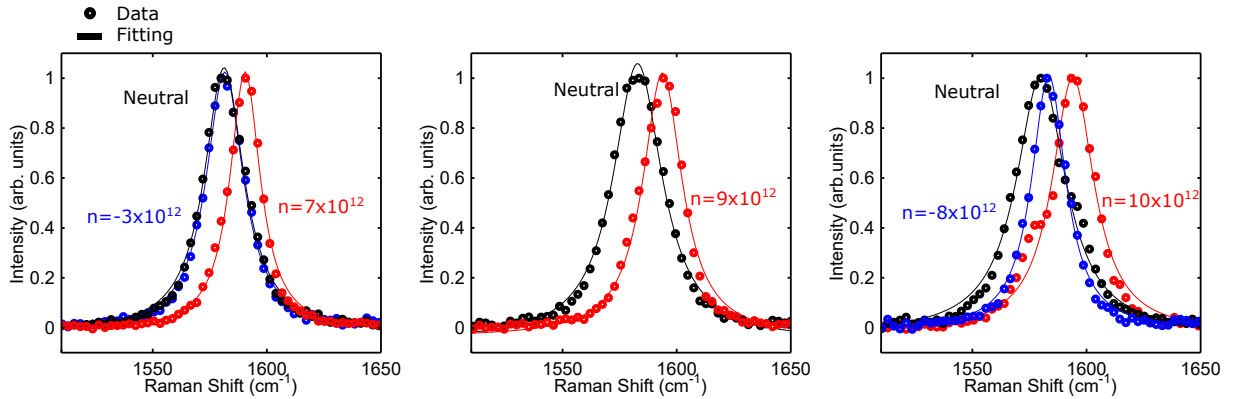
FIG. S5: **G-band fitting process for three magic-angle TBG samples.** Experimental data are represented by dots and the single-Lorentzian fitting by solid lines. We present data for n-doped (blue), neutral (black) and p-doped (red) configurations. The data are from three different magic-angle TBG samples. The graphics on the left shows the simplest result, where the doping behavior is clean and clear. The middle panel is from a device where, due to technical limitations, we could not achieve n-doping. The graphics on the right is from a sample where we observed a G-band shoulder in the case of p-doping. We believe the shoulder appears for devices with spatial inhomogeneities, while the fundamental result is well established by the single Lorentzian fitting (see red curve).

Theoretically, bilayer graphene C-C stretching present more than one peak due to symmetric and anti-symmetric vibrations within the two layers [15]. Even more peaks are expected in TBGs due to the zone-folded activated modes (see Fig. S3 and related text). However, the difference in frequency for these vibrations are negligible within the relatively small doping range around the charge neutrality point, as we address in the present work.
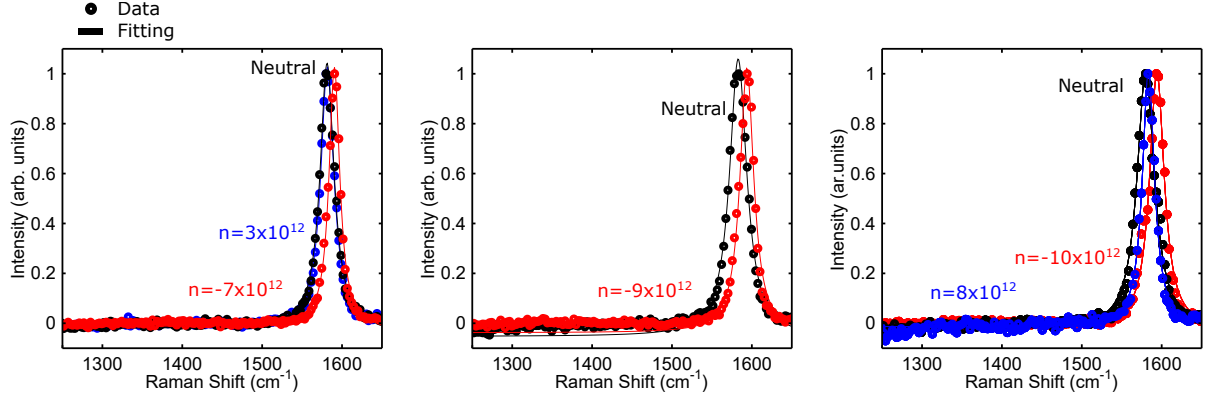
FIG. S6: **Absence of the defect-induced D band.** Same data as in Fig. S5 extended to include the D band frequency range ($\sim 1350\,\mathrm{cm}^{-1}$).

For this reason, Γ_G can be extracted form the G peak by using the single Lorentzian-line fitting, as discussed in [16] and shown in Fig. S5. Figure S6 shows the same data as in Fig. S5, with the frequency range including the region of the defect-induced D-band ($\sim 1350\,\mathrm{cm}^{-1}$). The absence of the D band shows the very low lever of defects in the graphene structure [17].

For completeness, Fig. S7 shows the measured 2D (or G′) peaks. Although the Kohn anomaly is expected to be strong at the K point, this effect is not strongly pronounced in this Raman feature, due to two aspects. First, the strongest electron-phonon coupling happens at the K point, and the 2D peak that can be accessed by Raman spectroscopy is not at the K point, but shifted away, where the effect is not so well pronounced [17]. Second, the 2D peak is not a one-scattering-event, but a combination of a large number of possible scattering events that fulfill internal multiple-resonance conditions in the electron-radiation plus electron-phonon coupling events, thus making the lineshape and analysis more complex [17]. This science has been addressed in [18].

Finally, 2D frequency vs G frequency mapping have been performed to evaluate frequency inhomogeneity in our sample. Thus, we provide 2D frequency vs G frequency plots over a $2 \times 3\,\mu$m area measured at the MATBG device, see Fig S8. The blue dots are the experimental data, while the red and black are arbitrary lines with 2.2 (strain) and 0.75 (doping) slopes, respectively [19]. The dots exhibit relatively small variations and do not spread over the lines, pointing out for small (insignificant) strain and doping. From Fig S8, inhomogeneties in the G band frequency do not account by more than $3\,\mathrm{cm}^{-1}$ increase in the overall G band

linewidth.

2.2. Device Characterization

Figure S9 shows schematics (a), Raman spectroscopy imaging (b) and a photo (c) of the actual device utilized in our experiemnt for the magic-angle TBG measurement.

We used back-top gate measurements on graphene to calibrate the ion gate capacitance. The top gate is the ionic liquid, and the back gate is the SiO_2/Si, with a known capacitance, see Fig. S10(a). Thus, we do graphene resistance ramps, varying both V_{ion} and V_{BG}. We evaluate the maximum graphene resistance peak position and plot in a graph of V_{ion} vs
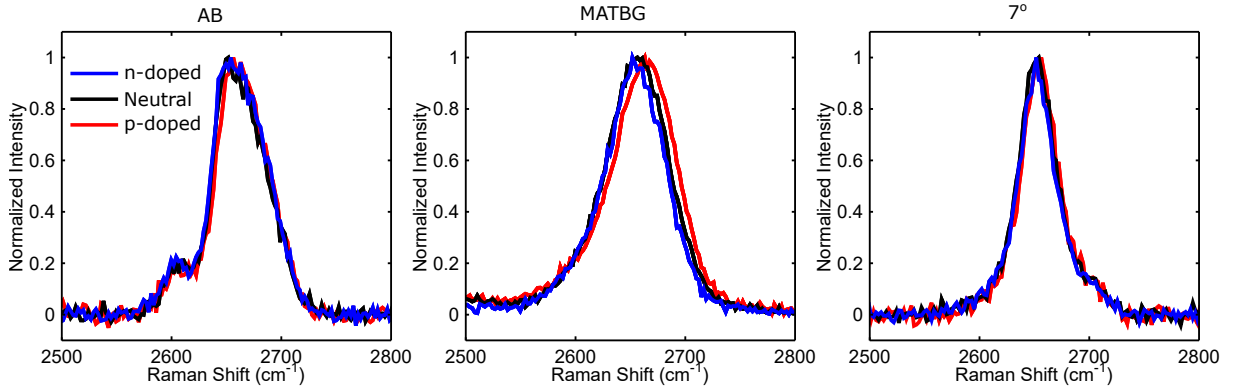
FIG. S7: **Raman spectra from the 2D-band for different doping and stacking.** Data are acquired for n-doped (blue), neutral (red) and p-doped (red) from AB (left panel), magic-angle (middle panel) and 7° (right panel) samples.
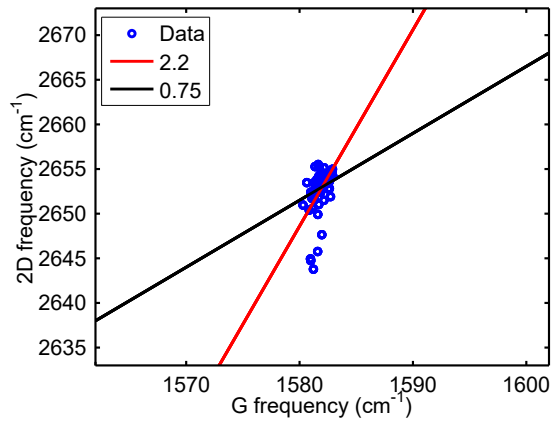
FIG. S8: **2D frequency vs G frequency plots.** The blue dots are the experimental data, while the red and black are arbitrary lines with 2.2 (strain) and 0.75 (doping) slopes, respectively.
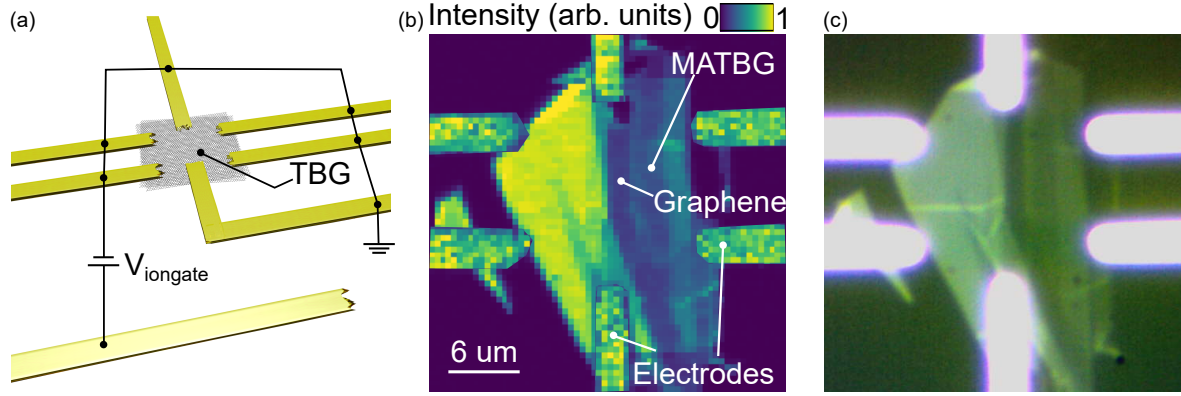
FIG. S9: **Device details.** **(a)** sketch of the device used in this work. **(b)** G band Raman map of the sample. **(c)** optical image of the sample. The iongate electrode is far from the TBG device and it cannot be seen in the (b,c) images.
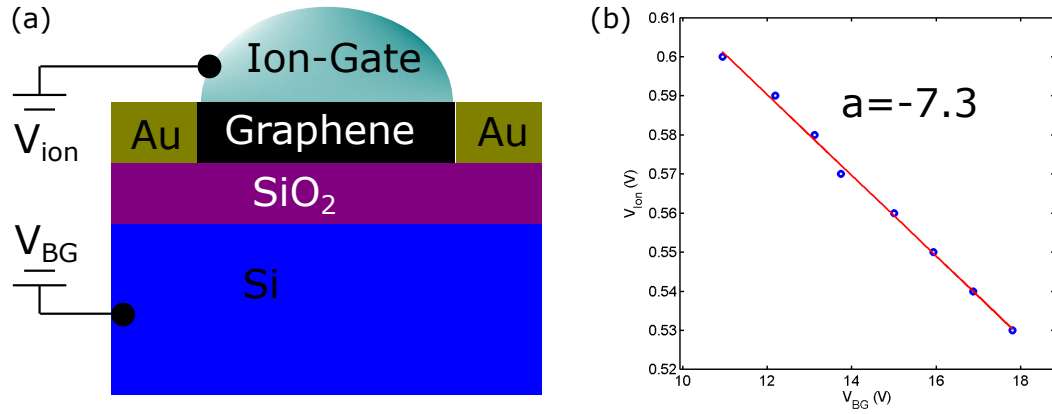
FIG. S10: **Capacitance calibration (a)** schematics of the device used to calibration the ion gate's capacitance. **(b)** V_{ion} vs V_{BG} plot exhibiting a calibration factor of -7.3.

V_{BG}, see panel Fig. S10(b). From the angular coefficient of this line, we can calculate the capacitance of the ion gate, and estimate the carrier concentration.

REFERENCES

* Electronic address: `jean-christophe.charlier@uclouvain.be`

† Electronic address: `adojorio@fisica.ufmg.br`

[1] Michael Lamparski, Benoit Van Troeye, and Vincent Meunier. Soliton signature in the phonon spectrum of twisted bilayer graphene. *2D Materials*, 7(2):025050, 2020.

[2] Andreij C Gadelha, Douglas AA Ohlberg, Cassiano Rabelo, Eliel GS Neto, Thiago L Vasconcelos, João L Campos, Jessica S Lemos, Vinícius Ornelas, Daniel Miranda, Rafael Nadas, et al. Localization of lattice dynamics in low-angle twisted bilayer graphene. *Nature*, 590(7846):405–409, 2021.

[3] Viet-Hung Nguyen, Dawid Paszko, Michael Lamparski, Benoit Van Troeye, Vincent Meunier, and Jean-Christophe Charlier. Electronic localization in small-angle twisted bilayer graphene. 2D Materials **8**, 035046 (2021).

[4] A. Lherbier, Simon M.-M. Dubois, X. Declerck, Y.-M. Niquet, S. Roche, and J.-C. Charlier, Phys. Rev. B **86**, 075402 (2012).

[5] V.-H. Nguyen, A. Lherbier, and J.-C. Charlier, 2D Materials **4**, 025041 (2017).

[6] G. Trambly de Laissardière, D. Mayou, and L. Magaud. Numerical studies of confined states in rotated bilayers of graphene. *Phys. Rev. B*, 86:125413, Sep 2012.

[7] Yuan Cao, Valla Fatemi, Shiang Fang, Kenji Watanabe, Takashi Taniguchi, Efthimios Kaxiras, and Pablo Jarillo-Herrero. Unconventional superconductivity in magic-angle graphene superlattices. *Nature*, 556(7699):43–50, 2018.

[8] Tommaso Cea, Niels R. Walet, and Francisco Guinea. Electronic band structure and pinning of fermi energy to van hove singularities in twisted bilayer graphene: A self-consistent approach. *Phys. Rev. B*, 100:205113, Nov 2019.

[9] Louk Rademaker, Dmitry A. Abanin, and Paula Mellado. Charge smoothening and band flattening due to hartree corrections in twisted bilayer graphene. *Phys. Rev. B*, 100:205114, Nov 2019.

[10] Tommaso Cea and Francisco Guinea. Band structure and insulating states driven by coulomb interaction in twisted bilayer graphene. *Phys. Rev. B*, 102:045107, Jul 2020.

[11] Zachary A H Goodwin, Valerio Vitale, Xia Liang, Arash A Mostofi, and Johannes Lischner. Hartree theory calculations of quasiparticle properties in twisted bilayer graphene. *Electronic Structure*, 2(3):034001, aug 2020.

[12] Cyprian Lewandowski, Stevan Nadj-Perge, and Debanjan Chowdhury. Does filling-dependent band renormalization aid pairing in twisted bilayer graphene? *npj Quantum Materials*, 6:82, Mar 2021.

[13] Tommaso Cea and Francisco Guinea. Coulomb interaction, phonons, and superconductivity in twisted bilayer graphene. *Proceedings of the National Academy of Sciences*, 118(32), 2021.

[14] Alexandr I Cocemasov, Denis L Nika, and Alexander A Balandin. Phonons in twisted bilayer graphene. *Physical Review B*, 88(3):035428, 2013.

[15] DL Mafra, P Gava, LM Malard, RS Borges, GG Silva, JA Leon, F Plentz, F Mauri, and MA Pimenta. Characterizing intrinsic charges in top gated bilayer graphene device by raman spectroscopy. *Carbon*, 50(10):3435–3439, 2012.

[16] T. C. Barbosa, A. C. Gadelha, D. A. A. Ohlberg, K. Watanabe, T. Taniguchi, G. Medeiros-Ribeiro, A. Jorio, and L. C. Campos 2D Materials **9**, 025007 (2022).

[17] A. Jorio, M. S. Dresselhaus, R. Saito, and G. Dresselhaus, *Raman spectroscopy in graphene related systems* (John Wiley & Sons, 2011).

[18] Eddwi H Hasdeo, Ahmad RT Nugraha, Mildred S Dresselhaus, and Riichiro Saito. Fermi energy dependence of first-and second-order raman spectra in graphene: Kohn anomaly and quantum interference effect. *Physical Review B*, 94(7):075104, 2016.

[19] Ji Eun Lee, Gwanghyun Ahn, Jihye Shim, Young Sik Lee, and Sunmin Ryu. Optical separation of mechanical strain from charge doping in graphene. *Nature Communications*, 3(1):1–8, 2012.